Available online at www.sciencedirect.com
SCIENCE DIRECT®

Physics of the Earth and Planetary Interiors 155 (2006) 104–119

PHYSICS OF THE EARTH AND PLANETARY INTERIORS

www.elsevier.com/locate/pepi

Improving seismic resolution of outermost core structure by multichannel analysis and deconvolution of broadband *SmKS* phases

David W. Eaton [a,b,*], J.-Michael Kendall [c]

[a] Department of Sciences Department, University of Western Ontario, 1151 Richmond Street, London, Ont., Canada N6A 5B7
[b] School of Cosmic Physics, Dublin Institute for Advanced Studies, 5 Merrion Square, Dublin 2, Ireland
[c] Department of Earth Sciences, University of Bristol, Wills Building, Queen's Road, Bristol BS8 1RJ, UK

Received 11 June 2005; received in revised form 15 October 2005; accepted 20 October 2005

Abstract

The presence of a thin ($\leq$12 km) layer atop the outermost core has important implications for the geodynamic and geomagnetic nature of the Earth, but detecting such a layer is difficult. *SmKS* seismic phases, which traverse the mantle as an *S*-wave and reflect $m-1$ times from the underside of the core–mantle boundary (CMB), offer a means to test proposed models since they are extremely sensitive to the velocity structure of the outermost core. To improve seismic resolution in this region, we have developed and validated a modified vespagram (slant stack) technique that makes use of phase-independent amplitude-envelope traces. Confidence limits on arrival-time and slowness estimates are obtained by bootstrap resampling. In order to mitigate the effects of waveform complexity and facilitate comparison between observed and modeled waveforms, we have used a simple deconvolution method similar to techniques used in exploration seismology. We have applied these methods to high-quality broadband recordings of three deep-focus earthquakes recorded by seismic arrays in Canada. Some of our measurements have turning depths <190 km in the outer core, a region of sparse coverage in previous global compilations of *SmKS* measurements. Based on the analysis of travel times, our data show that the *P*-wave velocity of the outermost core is PREM-like until the outer ~150 km or less, where it becomes much slower than PREM and most standard Earth models. Additionally, amplitudes of *S3KS*/*S4KS* phases relative to *SKKSac* are significantly larger than those predicted by standard models. Using reflectivity synthetic seismograms we show that no previous Earth model explains both our travel-time and amplitude anomalies. The superposition of a 12-km high-velocity and low-density layer at the top of the core, as proposed by Helffrich and Kaneshima [Helffrich, G., Kaneshima, S., 2004. Seismological constraints on core composition from Fe–O–S liquid immiscibility. Science 306, 2239–2242], improves the fit of waveform amplitudes regardless of the reference model.

Keywords: Outer core; *SmKS*; Seismic array methods; Deconvolution

1. Introduction

A thin boundary layer atop the outer core has been hypothesized based on indirect evidence (Lay and Young, 1990; Lister and Buffett, 1998; Braginsky, 1999). Such stratification requires dynamically stabilizing chemical heterogeneity (Stevenson, 1987) and, if present, would have profound implications for the geodynamo energy balance (Lister and Buffett, 1998). The accumulation of a metallic silicate phase at the top of the core (Buffett et al., 2000; Dubrovinsky et al., 2003) is one mechanism that could produce a thin layer (a few tens of kilometres thick) at the core–mantle boundary (CMB).

* Corresponding author. Tel.: +1 519 661 3190; fax: +1 519 661 3198.
E-mail address: deaton@uwo.ca (D.W. Eaton).

0031-9201/$ – see front matter © 2005 Elsevier B.V. All rights reserved.
doi:10.1016/j.pepi.2005.10.007

Recently, Helffrich and Kaneshima (2004) demonstrated that, for a plausible range of Fe–O–S compositions, a low-density layer could also exist as one of two immiscible fluid phases. Based on analysis of *P4KP* and *PcP* waveforms, they did not find any evidence indicative of such a layer. Using these phases, however, the predicted waveform expression is rather subtle. Additional seismic observations are required for conclusive validation or falsification of the existence of a thin layer at the top of the core.

Near the CMB, seismic velocity models (Fig. 1) show a large variability from one model to the next. This discrepancy reflects the weak sensitivity of most teleseismic phases to velocity structure of the outer-core region. Notable exceptions are so-called *SmKS* ($m = 1, 2, 3, \ldots$) waves, whose raypaths (Fig. 2) bottom in the outermost 200 km of the core. This class of teleseismic phase traverses the mantle as an *S*-wave, propagates within the outer core as a compressional wave, and undergoes $m-1$ underside reflections at the core–mantle boundary. *SmKS* arrival times are particularly sensitive to outer-core velocity structure (Choy, 1977; Garnero et al., 1993); consequently, a number of studies have employed differential times ($t_{S3KS} - t_{S2KS}$, $t_{S4KS} - t_{S3KS}$, etc.) to map seismic wave velocity in the outermost core.

Hales and Roberts (1971) compiled differential traveltime measurements of $t_{SKKS} - t_{SKS}$ and inverted the corresponding slowness data using the Herglotz-Wiechert procedure, yielding unexpectedly low velocities in the outermost core (Fig. 1). Lay and Young (1990) also reported evidence for a low-velocity layer in the outermost 50–100 km of the core, based on long-period recordings of events from the western Pacific. A compilation of mainly broadband waveform recordings of *SKS*, *SKKS* and *S3KS* by Souriau and Poupinet (1991) provided more uniform global coverage of these phases. They found that $t_{SKKS} - t_{SKS}$ traveltime residuals exhibit a prevailing contribution of long-wavelength heterogeneities in D″, whereas $t_{S3KS} - t_{SKKS}$ are much less sensitive to lower-mantle velocity anomalies. With the inclusion of additional waveform data to improve sampling of polar regions, Souriau et al. (2003) did not find evidence for heterogeneities deposited at the top of the core beneath the polar caps. Using a vespagram (stacking) method, Tanaka (2004) analyzed African broadband array recordings of *SmKS* waves that propagated

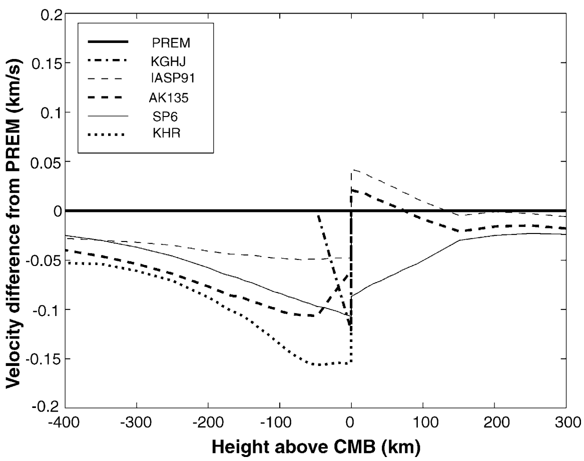

Fig. 1. Comparison of wavespeeds near the core–mantle boundary relative to PREM (Dziewonski and Anderson, 1981), for the following models: KGHJ (Garnero et al., 1993), IASP91 (Kennett and Engdahl, 1993), AK135 (Kennett et al., 1995), SP6 (Morelli and Dziewonski, 1993) and KHR (Hales and Roberts, 1976). *P* wavespeed is shown below the CMB and *S* wavespeed above.

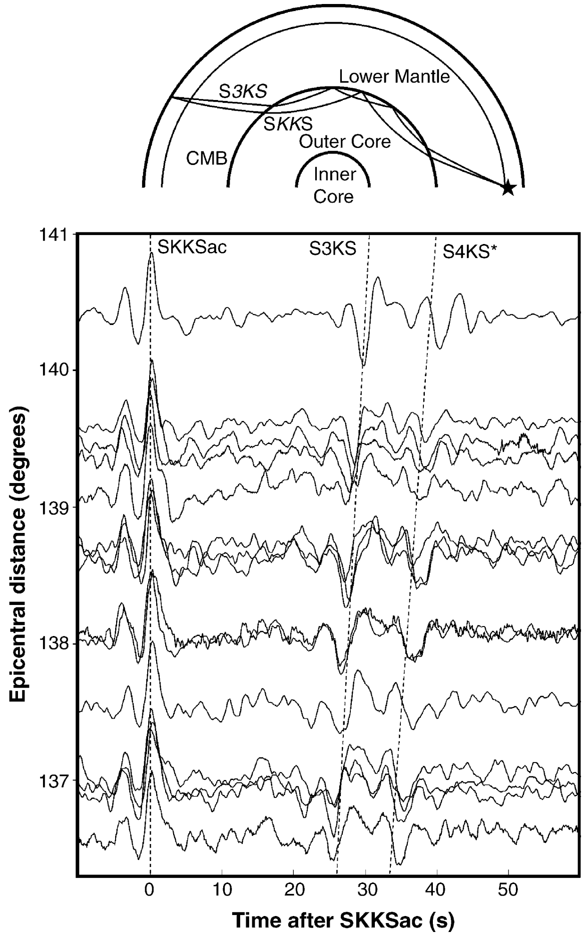

Fig. 2. *SKKS* and *S3KS* raypath geometry (top) and example record section (bottom), exemplifying broadband *SmKS* ($m = 2$–4) arrivals considered in this study. Seismograms are for event 2 recorded by the POLARIS Ontario array. Traces are aligned on *SKKSac*, and relative amplitudes are normalized with respect to the maximum amplitude of each trace. Dashed lines show predicted times based on IASP91 (Kennett and Engdahl, 1993). CMB denotes core mantle boundary.

beneath the southern Indian Ocean. While acknowledging the non-uniqueness of his interpretation, Tanaka (2004) argued that a low-velocity zone in the outer core best explains the anomalies, since the lower-mantle regions traversed by these *SmKS* phases exhibit only weak heterogeneity.

The widespread deployment of portable broadband arrays during the past decade, together with the advent of ambitious new continent-scale arrays such as USArray (Feder, 2003) and POLARIS (Eaton et al., 2005), provides motivation for further development of array techniques as well as methods that exploit the higher resolution afforded by broadband instruments. The purpose of this paper is two-fold: first, to develop new techniques for analysis of *SmKS* phases; secondly, to assess the detectability of a very thin layer at the top of the outer core though the use of such methods. We illustrate our approach using array recordings of several recent deep-focus earthquakes.

2. Characteristics of broadband *SmKS* recordings

The complete *SmKS* waveform is composed of an infinite series of multiply reflected waves (Choy, 1977). The time separation between consecutive *SmKS* arrivals decreases with m, and typically only a few of the lowest order terms in the series can be resolved as distinct pulses. In this paper, we use standard teleseismic notation (*SKS* and *SKKS*) to denote the first two terms in the *SmKS* series ($m = 1$, 2). Where a numerical value of $m > 2$ is written (e.g., *S3KS*, *S4KS*) a distinct arrival is implied. The label *SmKS* is used to represent either the waveform series taken as a whole, or a generic element of the series. We employ a nonstandard asterisk notation (e.g., *S4KS**) to denote the last distinctly discernible pulse (herein labeled the *terminal pulse*) in the *SmKS* series. The intent of this notation is to emphasize that the corresponding waveform is a composite pulse that incorporates contributions from higher order multiples (Choy, 1977).

For any given epicentral distance, the *SmKS* turning depth in the core decreases with increasing m. In principle, the terminal pulse (*SmKS**) therefore includes contributions from high-order multiple phases that bottom increasingly close to the CMB. However, since the amplitudes of *SmKS* modes tend to decrease rapidly with increasing m, higher order modes have a relatively minor effect on the *SmKS** pulse shape. Consequently, the *SmKS** arrival time is most sensitive to velocity near the turning depth of *SmKS*. Choy (1977) showed that summation of the first 15 modes is sufficient for waveform modeling to 125° epicentral distance.

Two other characteristics of *SmKS* waves are of practical importance. First, entry and exit points at the CMB converge with increasing value of m and/or with decreasing epicentral distance (Garnero et al., 1993). In many instances, the ray-theoretical CMB piercing points of distinct, observed *SmKS* phases fall within mutual Fresnel-zone limits. In this case, the two phases effectively sample the same paths outside the core, thus mitigating complications of velocity heterogeneity in shallower regions of the Earth. In addition, for each bounce, *SmKS* waves pass through an internal caustic (Kennett, 2001) that induces a Hilbert-transform phase shift. As noted by Souriau and Poupinet (1991), this characteristic has important ramifications for measuring differential times and should be accounted for in the method used to pick times for *SmKS* phases.

Many previous studies of *SmKS* have used intermediate- or long-period recordings in which the waveforms have a dominant period of about 10 s or more (e.g., Lay and Young, 1990; Garnero et al., 1993; Tanaka, 2004). In the common situation that this period is significantly greater than the earthquake rupture duration, recorded pulse shapes tend to have a simple shape (Kennett, 2001). One goal of our current work is to improve the seismic resolution of fine-scale structure of the outermost core by using broadband waveforms with a shorter dominant period. Although shorter period seismograms offer the potential for higher resolution of outer-core structure, they are sometimes characterized by an undesirably complex recorded waveform. Fig. 3 compares the resolving power of 10-s and 5-s source periods, based on the discernibility of distinct *SmKS* branches. For the 10-s period synthetic data, waveform interference obscures the arrival times of pulses that bottom in the top 100 km of the outer core, whereas for the 5-s period data reliable time picks can be made as close as 60 km below the CMB. These synthetic sections, as well as the synthetic seismograms discussed below, were computed using the reflectivity method (Fuchs and Müller, 1971). This method involves the computation of a reflectivity matrix and its integration over a user-specified slowness range, to produce a waveform that includes all possible reflected, transmitted and refracted waves.

Within user-specified limits of frequency and slowness, the reflectivity method synthesizes complete *SmKS* waveforms for all values of m. While this method requires the use of an earth-flattening approximation that breaks down with depth, the associated errors are

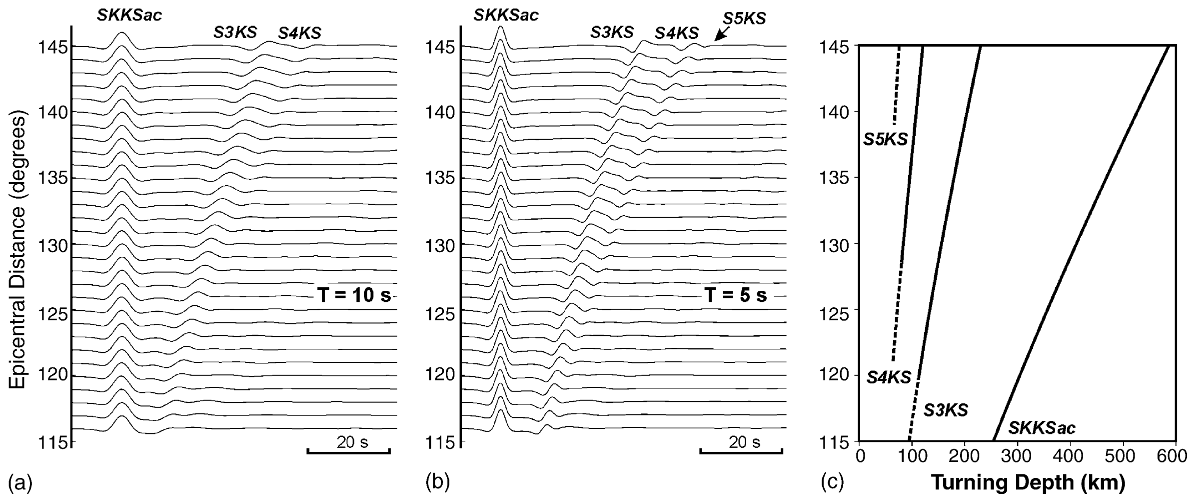

Fig. 3. (a) PREM reflectivity synthetics aligned on the *SKKSac* phase. Source pulse has a dominant period of 10 s. (b) As in (a), but with a dominant period of ∼5 s. (c) Ray-theoretical turning depth vs. epicentral distance for model PREM. Dashed lines indicate time picks that can be accurately discerned in the 5-s section, but not the 10-s section; solid lines indicate time picks that can be measured directly in both period bands.

negligible to depths that are well below the outer-core region of interest here (Müller, 1977). A more serious limitation of the reflectivity method is that it can only be applied to radially symmetric Earth models. Amplitude and traveltime distortions caused by lateral heterogeneity, especially in the lowermost mantle, are significant factors in the interpretation of individual seismograms and require alternative waveform simulation techniques (e.g., Garnero and Helmberger, 1995).

Fig. 4 shows a broadband recording that exhibits a complex source pulse. Despite the complicated pulse, the fidelity of the waveforms is evident from the nearly identical shapes of the *SKKS* and the Hilbert-transformed *S3KS* pulses. After two Hilbert transforms, the terminal pulse (*S4KS**) is similar, but not identical, to the *SKKS* pulse. The differences are due, at least in part, to contributions of higher order *SmKS* phases that alter the waveform characteristics of the terminal pulse.

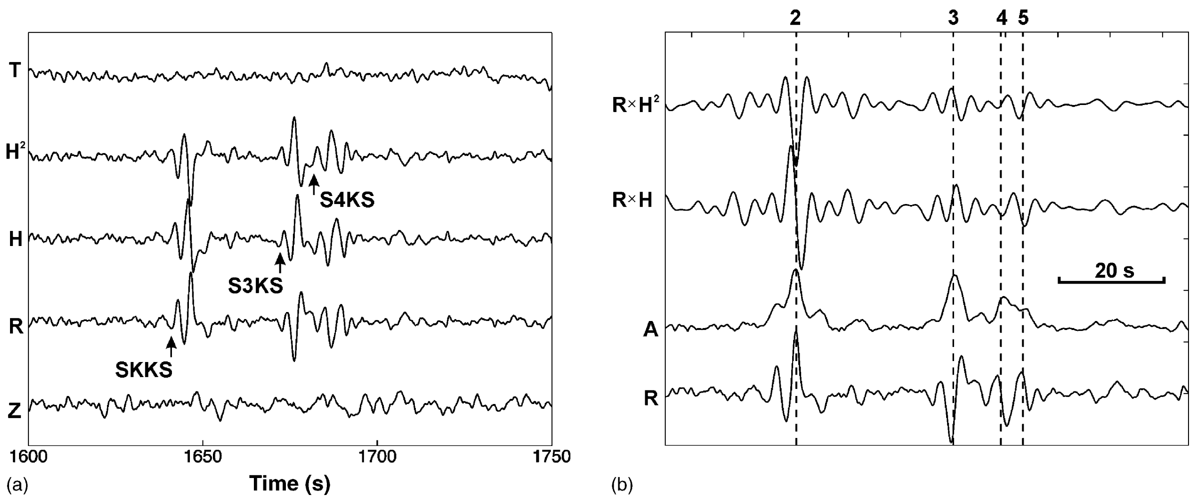

Fig. 4. (a) Observed *SmKS* waveforms for event 2 at station PLIO ($\Delta = 140.39°$). *Z*, *R* and *T* are the vertical, radial and transverse channels. *H* and H^2 are the Hilbert transform and double Hilbert transform of the radial component. Note the waveform similarity of *S3KS* and *SKKS* on the *H* and *R* components. The similarity begins to break down for *S4KS* (H^2) and *SKKS* (*R*). (b) Amplitude envelope (*A*) of the radial waveform, and cross-correlation of *R* with the *H* and H^2 waveforms. Note apparent alignment of local maxima for *A* and arrival times predicted by IASP91 (dashed lines). In this example, the widely used cross-correlation method successfully picks out the *S3KS* arrival, but misses *S4KS* (and *S5KS*), due to the presence of noise and a complex source waveform.

3. Application of amplitude-envelope calculations

Most previous studies of *SmKS* have employed a cross-correlation technique to measure differential times between *S3KS* and *S2KS*, *S4KS* and *S3KS*, etc. For the cross-correlation method, it is straightforward but necessary to take into account the Hilbert-transform phase shift between successive pulses. As discussed below, this approach sometimes fails in the case of noisy or complex waveform recordings. Here, we introduce an alternative method that is based on the so-called amplitude envelope:

$$A(t) = \sqrt{S^2(t) + H^2(t)}, \quad (1)$$

where $S(t)$ is the observed seismogram and $H(t)$ is its Hilbert transform. This signal-processing attribute has been widely used in seismic exploration since the late 1970s (Taner et al., 1979). Local maxima of the amplitude-envelope trace correspond to the most energetic arrivals and provide a practical datum for measuring both absolute and differential arrival times. The amplitude envelope is independent of wavelet phase; thus, for example, the amplitude envelopes of $S(t)$ and $H(t)$ are identical, an important advantage for the study of *SmKS* phases.

In Fig. 4b, the *S2KS*, *S3KS* and *S4KS** phases are easily recognizable in the amplitude-envelope trace. In addition, the time difference between successive local maxima in the envelope trace agrees rather well with expected time differences based on model IASP91 (Kennett and Engdahl, 1991). We note that, while cross-correlation of the observed seismogram with its Hilbert transform ($R \times H$) also produces a local maximum at nearly the same time as the corresponding peak of $A(t)$, the cross-correlation function is noisy and contains significant side lobes. Furthermore, the cross-correlation maximum corresponding to *S4KS** is ambiguous, probably due to the composite nature of this pulse. On the other hand, a clear *S4KS* peak (and the hint of an *S5KS** arrival) are apparent in the case of the amplitude-envelope trace, $A(t)$.

To assess the validity of the amplitude-envelope method for measuring differential times, Fig. 5 shows amplitude-envelope traces for reflectivity synthetics computed using model IASP91. The synthetic seismogram was computed using a 5-s period waveform and the section is aligned on the *SKKS* phase. Symbols superimposed on the traces show ray-theoretical arrival times, which track the *SKKS* peak amplitude at all epicentral distances. In the case of *S3KS* and *S4KS,* ray-theoretical times track the peak amplitude for distances greater than

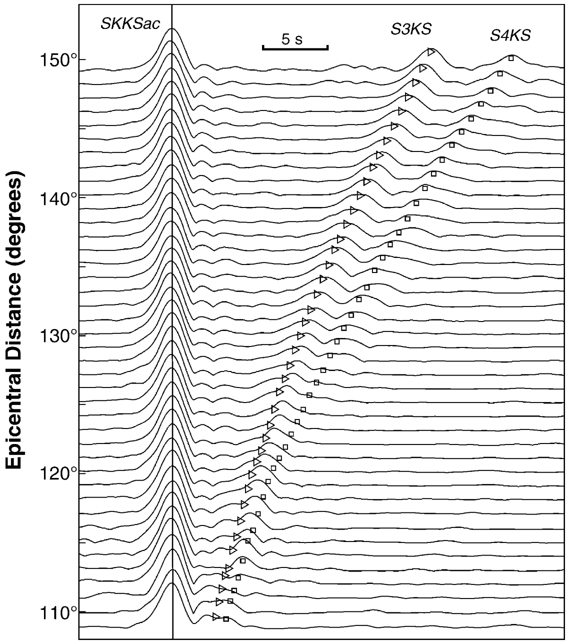

Fig. 5. Record section showing amplitude-envelope traces of reflectivity synthetics calculated for model IASP91 with a source period of 5 s. Seismograms are aligned on the *SKKSac* phase. Markers on each trace show ray-theoretical arrival times.

~115° and ~130°, respectively. At closer distances, where the separation between successive pulses is less than the dominant period of the waveform, waveform- and model-dependent merging and interference of the *SmKS* pulses occurs and the amplitude peak does not track the ray-theoretical arrival time. We have found that cross-correlation estimates of differential times are similarly distorted by interference between incompletely separated *SmKS* phases that comprise the terminal pulse.

Synthetic seismograms can be used to extend the observational range for *SmKS* time picks in order to include close epicentral distances where waveform interference effects are manifested, and thus improve velocity constraints for the outermost core. For consistency with previous studies, we have computed residuals with respect to the Preliminary Reference Earth Model (PREM; Dziewonski and Anderson, 1981). We have implemented this approach by: (1) computing synthetic seismograms for a standard Earth model, (2) measuring arrival times using the amplitude-envelope method described above and (3) subtracting these time picks from the observed arrival times to obtain residual times. This approach works best if the pulse shape is similar for both synthetic and observed waveforms. The next section outlines a deconvolution approach that we have used to achieve this.

4. Deconvolution

Detailed comparisons between observed and synthetic seismograms are hampered if the source-time function is complex, as in Fig. 4. Deconvolution methods, used routinely in exploration seismology, provide a possible solution to this problem. Deconvolution methods have been previously adapted for application to teleseismic problems (e.g., Bostock and Sacchi, 1997; Li and Nábelek, 1999; Neal and Pavlis, 2001). For stability, most methods require an a priori estimate of the source-time function. Difficulties arise if the deconvolution is applied to phases which have undergone differing degrees of anelastic attenuation (Neal and Pavlis, 2001).

For *SmKS* phases, the deconvolution problem can be posed in a particularly simple but effective manner using frequency-domain spectral normalization. In this study, we use the *SKKSac* waveform as a direct estimate of the source waveform, for both the observed and synthetic seismograms. An operator is then derived on a trace-by-trace basis that deconvolves the observed source using the modeled source pulse. This operator is then applied to the entire *SmKS* waveform to convert each pulse into a simpler shape. This approach is valid in cases where the source and path effects for *SKKSac* and *SmKS* are nearly the same, a condition that should be satisfied to a very good approximation if the CMB entry and exit points for these distinct teleseismic phases fall within their mutual Fresnel zones. The deconvolved seismic signal, $D(\omega)$, can be written as:

$$D(\omega) = \frac{W_D(\omega)S(\omega)}{\phi(\omega)}, \tag{2}$$

where $S(\omega)$ is the Fourier transform of the observed seismogram, $W_D(\omega)$ the spectrum of a 'design' wavelet (see below) and

$$\phi(\omega) = \max\{\hat{W}(\omega), c\hat{W}(\omega)\}. \tag{3}$$

Here, the spectrum of an a priori source wavelet is given by $\hat{W}$. A water level parameter, c, is introduced to stabilize the deconvolution in the presence of noise and the band-limited nature of the signal. A value of $c = 0.01$ was judged by visual inspection to give the best results.

There is considerable flexibility in the choice of design waveform. For example, obtaining a design waveform by isolating the *SKKSac* pulse in the synthetic seismogram reduces the deconvolution process to a so-called matched-filtering algorithm. This approach dramatically improves the fit between corresponding observed and synthetic traces, and may be especially useful as a pre-processing step before formal waveform inversion. On the other hand, selection of a design waveform that approximates a Dirac delta function results in so-called spiking deconvolution. This technique, in principle, provides the maximum possible resolution up to the Nyquist frequency.

The matched-filtering method is illustrated by the top four traces in Fig. 6. The observed source-time function (W_O) is estimated by applying a unit-amplitude 'boxcar' gate function to the observed seismogram (O). The gate function is centered on *SKKSac* and uses a 2-s Hanning taper at each end. The width of the gate function is selected interactively to include the entire *SKKSac* pulse. The design wavelet (W_1) is obtained by applying a similar gate function to the synthetic seismogram. After application of the deconvolution operator, the deconvolved *SKKSac* waveform (D_1) is aligned with, and nearly identical to, the modeled waveform, as expected. Similarly, the deconvolved *S3KS* and *S4KS** waveforms are shifted in time by the same amount as the *SKKSac* waveform, and more closely resemble the shape of the corresponding pulses in the synthetic seismogram. However, since each trace in Fig. 6 is scaled by the peak *SKKSac* amplitude, it is clear that *S3KS* and *S4KS** amplitudes are substantially greater than the PREM synthetics. Possible reasons

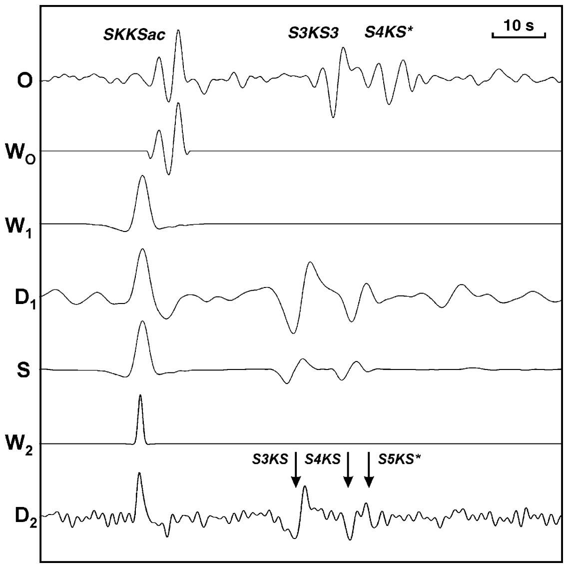

Fig. 6. Deconvolution method. Observed seismogram (O) is radial component for event 2 at station PLIO ($\Delta = 140.39°$). Estimated source wavelet (W_O) is obtained by applying a gate function to the seismogram in order to isolate the *SKKSac* arrival. First design wavelet (W_1) is obtained in a similar manner from the PREM synthetic seismogram (S). Deconvolved trace D_1 is obtained by applying the $W_O \rightarrow W_1$ matched-filtering operator to O. Spiking deconvolution wavelet (W_2) has a Gaussian spectrum with a centre frequency of 0.05 Hz and a standard deviation of 0.5 Hz. D_2 is obtained by applying the $W_O \rightarrow W_2$ matched-filtering operator to O.

for this large discrepancy in the relative amplitudes of the *SmKS* phases are discussed in the next section. This example serves to illustrate the utility of matched deconvolution as a tool for making such comparisons.

An example of (pseudo-)spiking deconvolution is presented in the lower two traces of Fig. 6. In this case, the design wavelet is a Gaussian pulse with a width of 1.8 s. This design wavelet was used rather than a Dirac delta function, since the latter resulted in an uninterpretable noisy output. As indicated by the arrows, the extended bandwidth provided by pseudo-spiking deconvolution enables better resolution of the *SmKS* series, including a distinct apparent *S5KS** pulse. Unfortunately, pseudo-spiking deconvolution imposes rather stringent requirements for high signal-to-noise ratio and yielded generally unsatisfactory results when applied to the majority of the waveform observations in this study. Hence, only matched deconvolution is presented in the examples below.

5. Array-based measurements of *SmKS* parameters

Observations of teleseismic *SmKS* phases using a closely spaced network of stations enables the use of array methods to analyze these signals. In particular, vespagrams, slant-stack diagrams of seismic energy (Rost and Thomas, 2002), can be used to improve the resolution of arrival time and slowness. Tanaka (2004) introduced the use of vespagrams to measure arrival time and slowness for *SmKS* phases. To account for the Hilbert-transform phase shift between *SKKS* and *S3KS*, Tanaka (2004) calculated separate vespagrams for each phase. Here we have modified this technique in two ways. First, we compute vespagrams by slant-stack processing of amplitude-envelope traces, rather than the actual seismograms. This approach exploits the phase-independent properties of the amplitude envelope, thus permitting the display and picking of all resolvable *SmKS* phases on a single vespagram. Secondly, we apply the matched-deconvolution procedure prior to computation of the vespagram. This mitigates undesirable 'ringy' characteristics of some broadband source waveform and permits a more direct comparison between the observed and synthetic data. For each phase, the arrival-time and slowness parameters are extracted from the vespagram by an automatic search for the corresponding local maximum point. Confidence limits on these parameters are obtained using a bootstrap resampling procedure (see below).

Table 1
Events used in this study

Event	Location	Date	Latitude (°)	Longitude (°)	Depth (km)	Mw
1	Fiji	1997/09/04	−26.45	178.52	621.0	6.8
2	Sumatra	2004/07/25	−2.68	104.38	600.5	7.3
3	Celebes Sea	2005/02/05	5.45	123.63	529.1	7.1

We have applied this modified vespagram procedure to *SmKS* phases excited by three deep-focus earthquakes (Table 1), recorded by broadband stations in Canada (Fig. 7). Event 1 was recorded during the TW ∼ ST

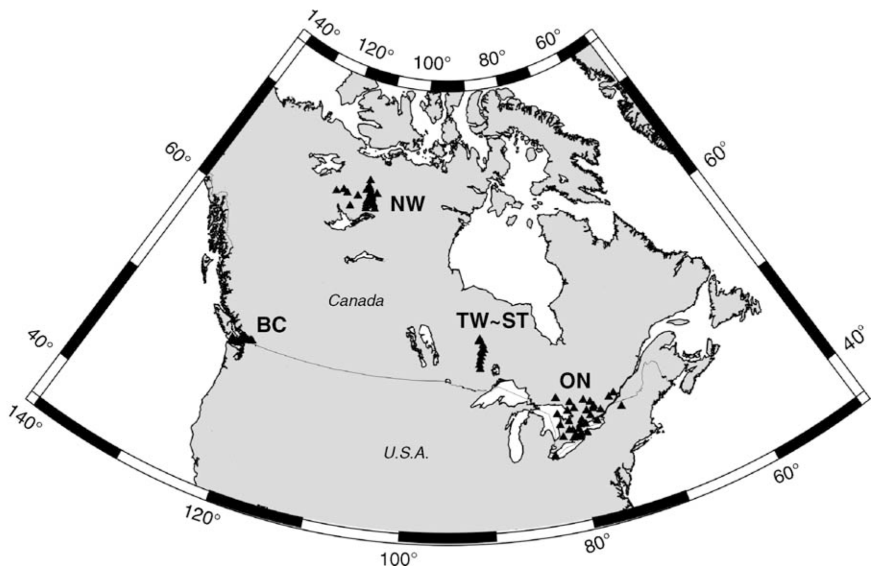

Fig. 7. Map of seismograph stations used in this study, indicating names of arrays used.

experiment (Kendall et al., 2002); recordings of events 2 and 3 were obtained from POLARIS network stations (Eaton et al., 2005) in western, northern and east-central Canada. Figs. 8–10 show examples of record sections and corresponding vespagrams for observed, synthetic and deconvolved data. The synthetic seismograms were computed using Harvard CMT double-couple source mechanisms, with a 5-s source pulse. Trace-by-trace matched filtering was applied to the observed data using the procedure described above. This deconvolution process causes the *SKKS* waveform to be virtually the same as the modeled *SKKS* arrival on the PREM synthetic, in terms of pulse shape, arrival time and slowness. After deconvolution, the *S3KS** pulse more closely resembles the character of the corresponding waveform on the synthetic record section, but the relative arrival time and slowness (with respect to the recorded *SKKS* arrival) are preserved to within confidence limits. This process sometimes slightly changes the slownesses of *SmKS* pulses relative to each other; this is mainly due to the alignment of the *SKKS* pulse with PREM as a result of matched deconvolution, which removes some of the trace-to-trace "jitter" that can otherwise degrade the vespagram stack. This approach thus enables a more robust determination of residual time than is possible with conventional techniques, and also furnishes relative slowness and amplitude information. Arrival-time and slowness measurements are summarized in Table 2.

We used a bootstrap resampling technique (Chernick, 1999) to estimate confidence limits for the time and slowness estimates. This technique makes no a priori assumptions about the statistical distribution of the recorded

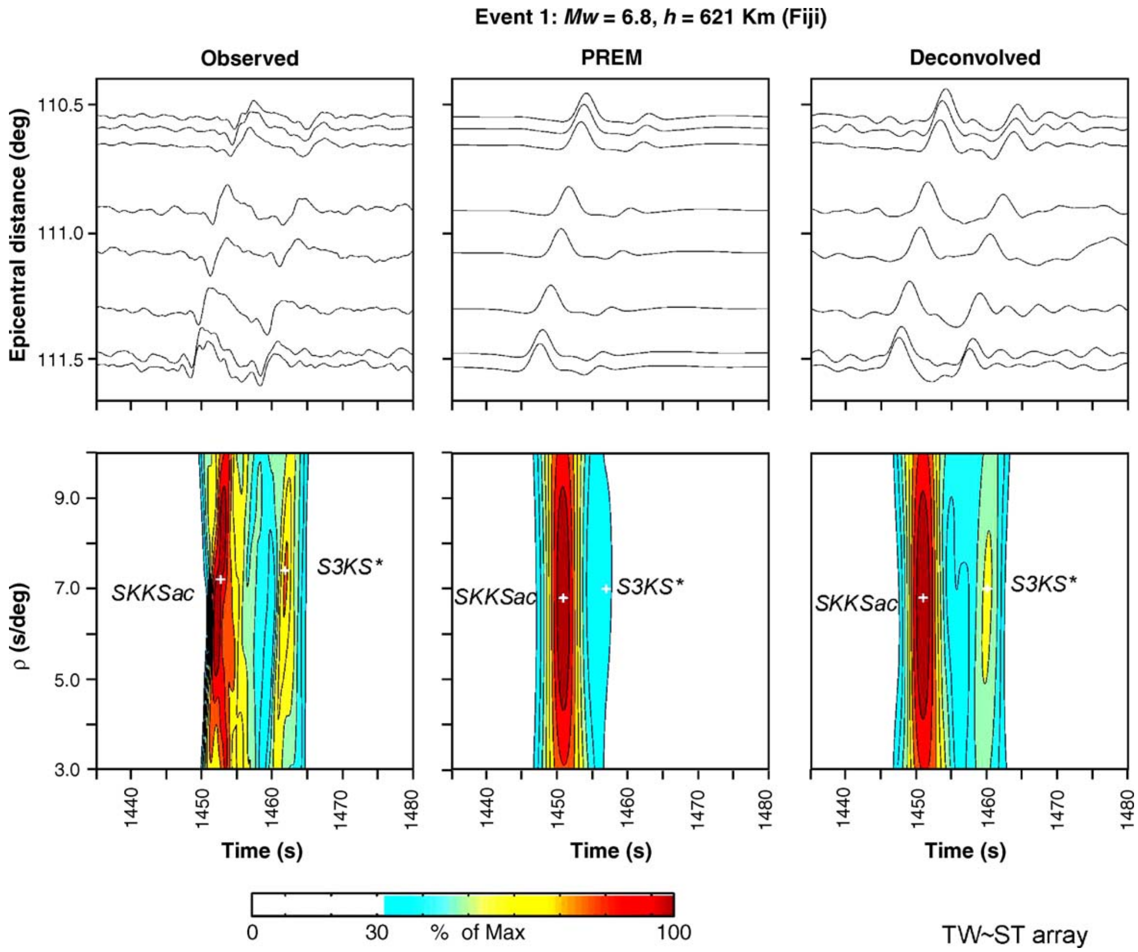

Fig. 8. Observed, synthetic and deconvolved record sections and vespagrams (slant stacks) for event 1, recorded by TW ∼ ST stations in central Canada. Seismic trace amplitudes are normalized with respect to the maximum amplitude of each trace. Vespagrams were computed using the amplitude envelopes of the traces in the corresponding upper panels. The deconvolution process has rendered the *SmKS* waveforms more similar to the synthetic traces. Crosses indicate local maxima in stack amplitude, corresponding to *SKKSac* and *S3KS** phases. Observed *S3KS** phase is delayed by 3.3 ± 1.3 s relative to PREM. Note the poor slowness resolution in this case, due to the relatively limited aperture of the array of stations.

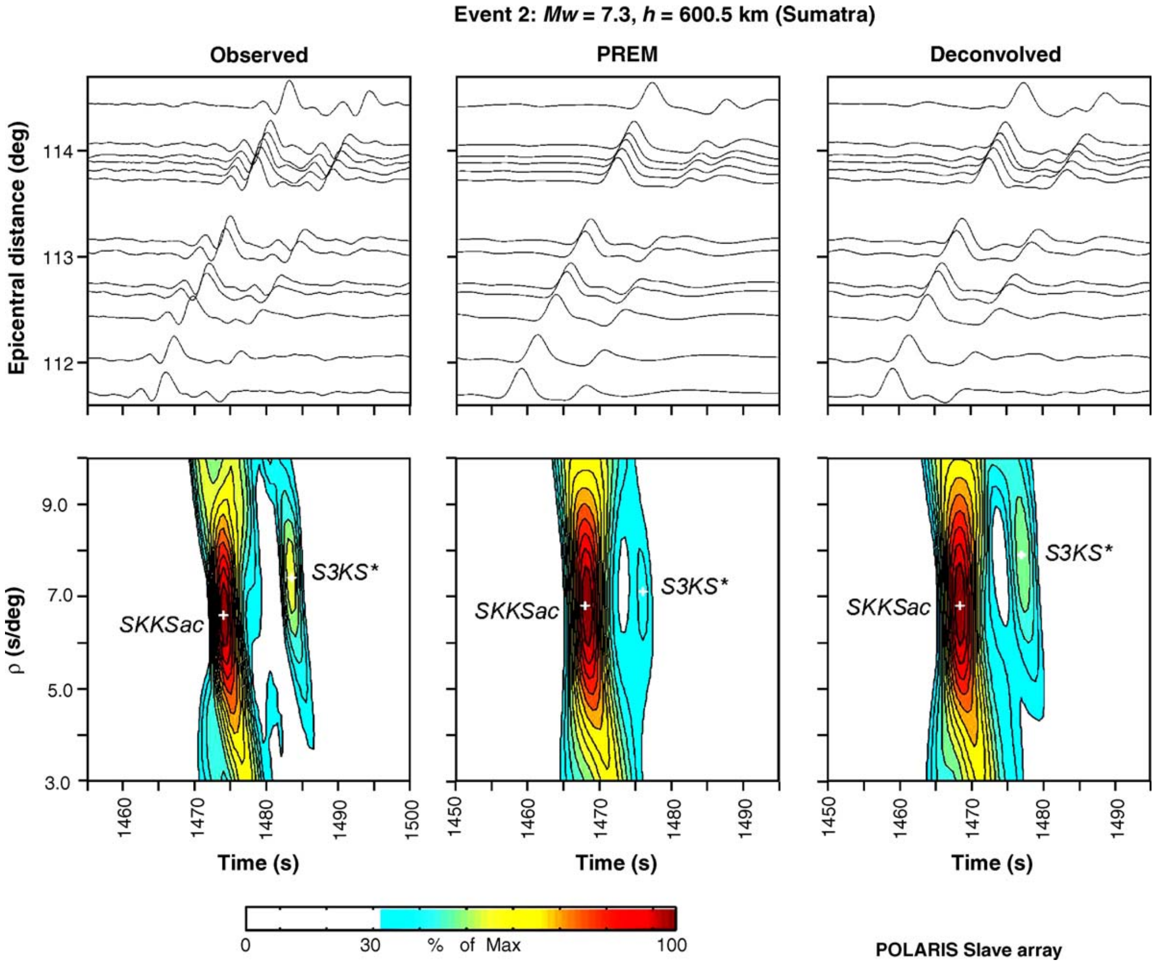

Fig. 9. Observed, synthetic and deconvolved record sections and vespagrams (slant stacks) for event 2, recorded by POLARIS stations in northern Canada (NW). Seismic trace amplitudes are normalized with respect to the maximum amplitude of each trace. Vespagrams were computed using the amplitude envelopes of the traces in the corresponding upper panels. The deconvolution process has rendered the *SmKS* waveforms more similar to the synthetic traces. Crosses indicate local maxima in stack amplitude, corresponding to *SKKSac* and *S3KS** phases. Observed *S3KS** phase is delayed by 0.8 ± 0.4 s relative to PREM.

Table 2
Summary of array-based *SmKS* observations

Event	Array[a]	Latitude[b] (°)	Longitude[b] (°)	Epicentral distance (°)	Back-azimuth (°)	Phase[c]	Time residual[d] (s)	Amplitude residual	Slowness residual[d] (s/deg)
1	TW (8)	51.348	−90.363	111.07	253.6 ± 0.6	3–2	3.3 ± 1.3	0.21 ± 0.04	0.0 ± 1.7
2	NW (13)	64.337	−111.039	113.21	322.2 ± 1.1	3–2	0.8 ± 0.4	0.09 ± 0.01	0.6 ± 0.5
2	BC (13)	48.877	−123.485	118.52	303.1 ± 0.9	3–2	0.7 ± 1.5	0.01 ± 0.06	0.1 ± 2.6
2	ON (21)	44.149	−79.046	138.33	355.6 ± 6.0	3–2	-0.2 ± 0.9	0.12 ± 0.05	-0.1 ± 0.9
2	ON (21)	44.149	−79.046	138.33	355.6 ± 6.0	4–3	1.7 ± 1.3	0.07 ± 0.07	0.3 ± 1.2
3	ON (13)	44.409	−78.881	126.57	330.6 ± 3.8	3–3	0.3 ± 0.8	0.09 ± 0.04	0.7 ± 0.7

[a] TW denotes TW ~ ST experiment; POLARIS arrays are denoted as follows: NW, Northwest Territories; ON, Ontario; BC, British Columbia. Value in parentheses indicates number of seismograms.

[b] Array centroid location.

[c] 3–2 denotes *S3KS–SKKSac*; 4–3 denotes *S4KS–S3KS*.

[d] Uncertainties based on bootstrap 95% confidence limits using deconvolution method described in text.

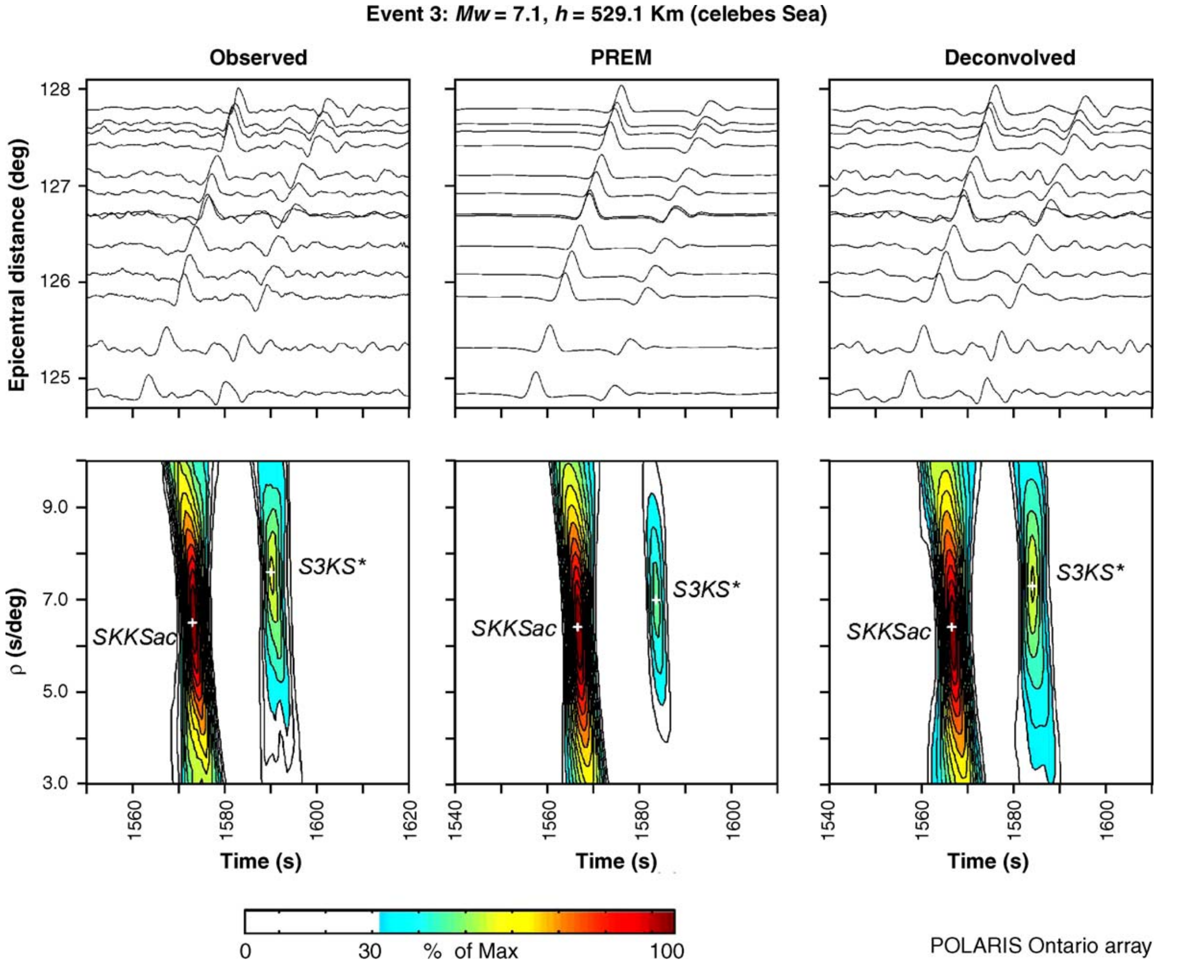

Fig. 10. Observed, synthetic and deconvolved record sections and vespagrams for event 3, recorded by POLARIS stations in Ontario (ON). Seismic trace amplitudes are normalized with respect to the maximum amplitude of each trace. Vespagrams were computed using the amplitude envelopes of the traces in the upper panels. Crosses indicate local maxima in stack amplitude, corresponding to *SKKSac* and *S3KS** phases. Observed *S3KS** phase is delayed by only 0.3 ± 0.8 s relative to PREM, but has a higher amplitude than predicted.

amplitudes. Confidence regions were determined by computing 1000 bootstrap averages of the slant-stack amplitude at the local maximum point corresponding to the desired *SmKS* arrival. The 1000 amplitude values were then arranged in ascending order, and the 50th smallest amplitude used to establish a lower limit on the peak amplitude value at the 95% confidence level. This value was then used as a contour level to enclose the (roughly elliptical) 95% confidence region on the vespagram in the neighbourhood of the local maximum.

Array-derived differential time and amplitude residuals with respect to PREM are graphed in Fig. 11. The observed values are plotted with respect to the mean turning depth below the CMB. This depth was calculated using the epicentral distance at the centroid of the array, and for the two *SmKS* phases used to obtain the differential time. For comparison with previous *SmKS* measurements, Fig. 11 also shows $t_{S3KS^*} - t_{SKKS}$ measurements compiled by Souriau et al. (2003) and Sylvander and Souriau (1996). Their data are sparse in the outermost 190 km of the core, but for mean turning depths >190 km our data fall within the scatter of these previous observations. For mean turning depths <150 km, our data indicate positive residuals of 0.8 ± 0.4 to 3.3 ± 1.3 s. These positive residuals are in qualitative agreement with previously proposed models for the outermost core, which consistently show velocities lower than PREM in the outer part of the core (Fig. 1).

The elongation of contours parallel to the slowness axis (Figs. 8–10) reflects large uncertainties in slowness (Table 2). Although our slowness measurements are in generally good agreement with predicted values, the large uncertainties preclude definitive inferences about velocity structure based on the measured slowness data

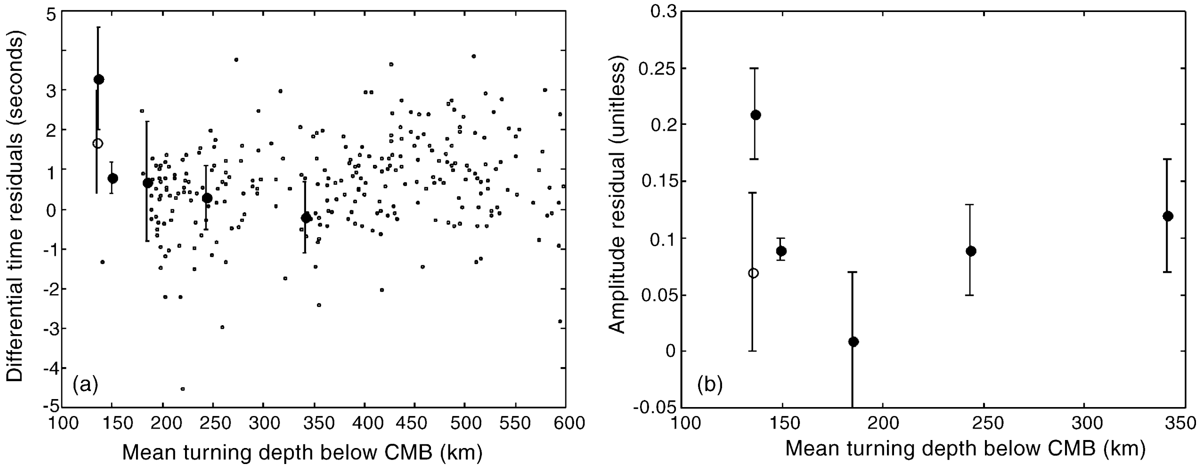

Fig. 11. (a) Graph of residual $t_{S3KS} - t_{S2KS}$ values vs. average turning depth, compared with data previously compiled by Sylvander and Souriau (1996) and Souriau et al. (2003). Open circle is for *S4KS**–*S3KS* measurements, and filled circles are for *S3KS**–*SKKS* measurements. Error bars represent 95% confidence limits from bootstrap resampling. Previous measurements (small dots) used a cross-correlation method. Measured times are residuals with respect to PREM. Our data fall (circles) within the scatter of previous results, with the exception of three measurements at turning depths <190 km. (b) Amplitude residual with respect to PREM. Positive values imply slower-than-predicted decay of *SmKS* amplitudes. Note that the two observations with a mean turning depth of ∼130 km are for different events.

alone. On the other hand, observed amplitude residuals exhibit statistically significant positive values (Fig. 11b) that warrant further analysis. The amplitude residual is here defined as a unitless parameter given by

$$\Delta A = \left(\frac{A_{SmKS}}{A_{SnKS}}\right)_{\text{obs}} - \left(\frac{A_{SmKS}}{A_{SnKS}}\right)_{\text{pred}}, \qquad (4)$$

where $n = m - 1$. Since *SmKS* phases undergo multiple underside reflections at the CMB, the rate of decay of the *SmKS* series is sensitive to the velocity gradient in the outermost core as well as energy partitioning at the CMB (i.e., the reflection coefficient).

6. Discussion

In the case of time differences calculated using two *SmKS* phases with widely separated entry/exit points at the CMB, Garnero and Helmberger (1995) cautioned that strong lower-mantle heterogeneity can lead to significant traveltime and amplitude artifacts that, if unrecognized, could map erroneously into outer-core velocity structure. This cautionary conclusion is particularly applicable to instances where CMB entry or exit points of *SmKS* rays are located within or near an ultra-low velocity zone (ULVZ) in the lowermost mantle. These findings are supported by extensive single-station data compiled by Souriau and Poupinet (1991), which show substantially greater regional variations of traveltime residuals in the case of *SKKS*–*SKS* than for *S3KS*–*SKKS*. Tanaka (2004) applied array techniques to selected *S3KS* and *SKKS* phases that sample 'normal' lower mantle beneath the Indian Ocean, and argued that the lower-mantle contributions to *S3KS*–*SKKS* traveltime residuals in his dataset are insignificant. There remain, however, considerable uncertainties in the magnitude and distribution of velocity anomalies in the lower mantle based on global tomographic models (e.g., Mégnin and Romanowicz, 2000). We suggest that analysis of a globally representative sampling of *SmKS* phases is preferable to interpretations based on a few measurements that pass through inferred 'normal' lower mantle, since: (1) a global approach would be model-independent; (2) the lower mantle contains short-wavelength heterogeneity that is not represented by global tomographic models (Garnero, 2000); (3) given sufficient global coverage of *SmKS* observations, biases produced by positive and negative lower-mantle anomalies should cancel out. The use of broadband arrays offers the additional promise of better-resolved and more robust results, compared with previously compiled single-station measurements.

For the *SmKS* phases considered in this study, CMB entry and exit points are located within or near several known large-scale velocity anomalies in the lower mantle, of both negative and positive polarity (Fig. 12). For example, CMB entry points for event 1 are located at the southern edge of lower-mantle low-velocity region beneath the southern Pacific (Fig. 12d). It is likely that *S*-wave passage through this region contributes to part of the previously noted large positive traveltime residual of 3.3 ± 1.3 s, due to the more oblique path of (and lower velocities intersected by) rays associated with *S3KS*. On the other hand, CMB entry and exit points for

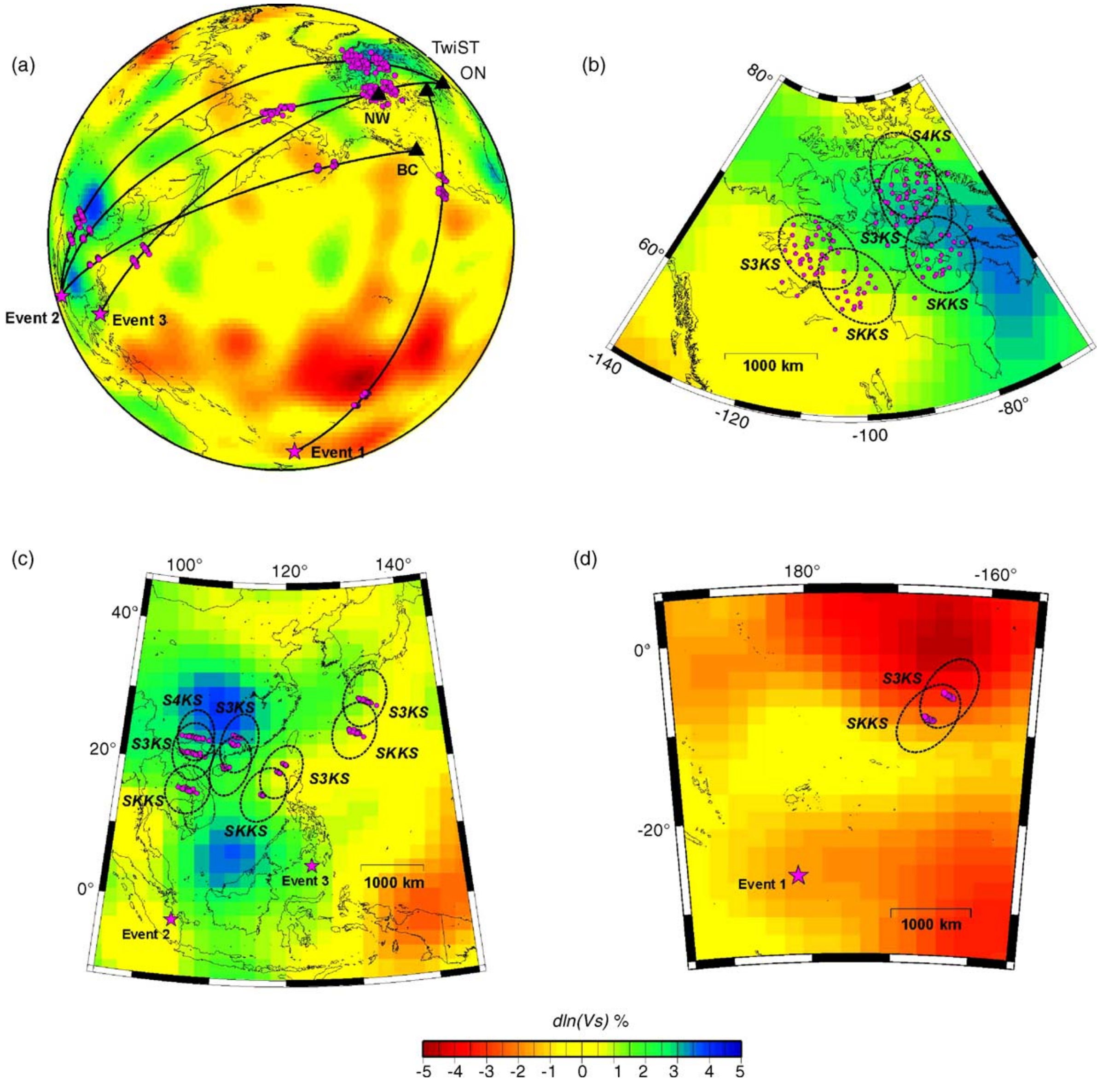

Fig. 12. (a) Great circle paths from events to array centroid locations, and CMB entry and exit points (small circles). Background colors show mantle *S*-wave velocity perturbations in the D″ region (2850 km depth), from global tomographic model SAW24B16 (Mégnin and Romanowicz, 2000). Rays from event 1 pass through ultra-low velocity D″ region in the south Pacific. Rays from event 2 pass through high-velocity D″ beneath southeast Asia and North America. (b) Enlargement of CMB exit points beneath North America. Dashed ellipses show example Fresnel zones. (c) Enlargement of CMB entry points beneath Asia. (d) Enlargement of CMB entry points beneath the south Pacific. Dashed ellipses indicate representative Fresnel zones for 5-s period.

event 2 overlap with high-velocity regions in the lower mantle beneath China and North America, respectively (Fig. 12). In the case of this event, we observe a positive traveltime residual of 1.7 ± 1.3 s for *S4KS–S3KS*, despite the competing influence of the high-velocity lower-mantle anomalies. Thus, while lower-mantle heterogeneity is clearly an important factor, velocities much slower than PREM in the outer 150 km of the core appear necessary to fit our data. We acknowledge, however, that our present dataset is not a globally representative sampling. The analysis below is thus intended to explore the sensitivity of our array methods to previously conjectured layering of the outermost core; definitive conclusions concerning the 1D velocity structure of the outermost core must await the acquisition of a more globally extensive dataset.

Different models for outer-core velocity structure have been proposed in the literature, some based primarily on the analysis of *SmKS* phases. Rather than develop a new model that best fits our rather limited current data, we confine our attention here to representative existing velocity models and perturbations thereof. The published velocity models considered here are: KGHJ (Garnero et al., 1993), IASP91 (Kennett and Engdahl, 1991), AK135 (Kennett et al., 1995), SP6 (Morelli and Dziewonski, 1993) and KHR (Hales and Roberts, 1971). For models that specify core velocities only (KGHJ and KHR), we used the PREM model for the mantle. For all models, reflectivity synthetics were computed in order to obtain *S3KS* and *SKKSac* residuals, using the vespagram technique described above. Array calculations for the synthetic data were made using a five-trace moving window spanning 4° in epicentral distance. A best-fit line was then obtained for each of the modeling results.

From top to bottom, the models in Fig. 13 are arranged in order from the fastest to the slowest velocities in the outer 150 km of the core. Of the models considered here, model KGHJ (Garnero et al., 1993) gives the best fit to the time residuals in our dataset. This model is identical to PREM except for a reduction in core wavespeeds in the top 50 km (Fig. 1). Indeed, this model is unique in predicting a decreasing time residual with increasing turning depth in the top 350 km of the core, as indicated by our data. Models AK135, SP6 and KHR predict larger time residuals than our data, whereas IASP91 fits the overall trend of the Souriau et al. (2003) data compilation reasonably well (cf. Fig. 11). Model KHR (Hales and Roberts, 1971) predicts a higher ratio of *S3KS* to *SKKSac* amplitude than the other models, and gives the best fit to our amplitude-residual data. In general, for regions deeper than 150 km in the core, the faster models give a better fit to the time residuals, whereas the slower models give a better fit to the amplitude residuals.

Other factors may affect amplitude residuals, including the Q-structure of the outer core and aforementioned lateral heterogeneity in the lowermost mantle. Q models for the outer core exhibit considerable scatter, but most indicate that $Q_P > 1000$ for $f = 0.2$ Hz (Tanaka and Hamaguchi, 1996). For the case of simple constant-Q models of the outer core, our modeling results (not shown) indicate that *SmKS* amplitude residuals (Eq. (4)) are relatively insensitive to Q_P for the range $300 < Q_P < 10{,}000$, since a similar level of anelastic attenuation characterizes successive *SmKS* phases.

Fig. 13 also shows results for models perturbed with a 12-km thick low-density layer at the top of the core. This thickness represents an approximate upper limit for a low-density layer at the top of the core, the mass of which balances the excess mass of the inner core (Helffrich and Kaneshima, 2004). Three specific scenarios are depicted: (1) the low-density (high-temperature) end-member of immiscible fluid layers proposed by Helffrich and Kaneshima (2004), with $V_p = 8.36$ km/s and $\rho = 8.97$ Mg/m^3; (2) a 10% reduction in ρ (with respect to PREM) with no change in V_p; (3) a 10% reduction in both ρ and V_p, with respect to PREM. The results for these three scenarios are indicated as thin, dashed and dotted lines, respectively, in Fig. 13. For case 2 (a thin layer with 10% reduction in ρ but no change in velocity), the differences are negligible. As expected, this layer produced no appreciable difference in the time residual, and only very slight differences in the amplitude-residual curves. Since the amplitude differences are less than the uncertainty in our array measurements, it seems unlikely that such a layer could be detected seismically. We comment, however, that the presence of a compositionally distinct low-density layer without any accompanying velocity signature seems improbable. For case 3 (a thin layer with 10% reduction in both ρ and V_p), severe waveform distortions due to thin-bed interference effects rendered accurate phase identification impossible for the two fastest models (PREM and KGHJ), and a degradation of the fit for the other models. For case 1, a thin S-rich fluid layer with composition and properties given by Helffrich and Kaneshima (2004), we observe a slight improvement in the overall fit for both time and amplitude, regardless of reference model.

To illustrate the detailed effects on pulse shape of thin layer, Fig. 14 compares synthetic *S3KS* and *S4KS** waveforms with an individual observed seismogram. Bold traces correspond to unperturbed reference models listed above. Synthetic traces that are plotted as dashed lines correspond to models containing a thin layer, with velocity and density as in case 1. All traces are normalized by the peak amplitude of the *SKKSac* pulse. Regardless of the starting model, the insertion of a thin, high-velocity layer produces an increase in the amplitude of *S3KS* and *S4KS** (relative to *SKKSac*), and a decrease in the time separation between the pulses. The amplitude increase is qualitatively consistent with our amplitude residuals; the decrease in *S3KS*–*S4KS* pulse separation is inconsistent with our positive time residuals at shallow turning depth. This implies that such a layer, if present, would represent a high-velocity lid above a layer of reduced wavespeed. Finally, we note that the presence of a high-velocity lid leads to a discernible phase shift that is manifested by increasing asymmetry (‘front-loading’) of the pulse. This

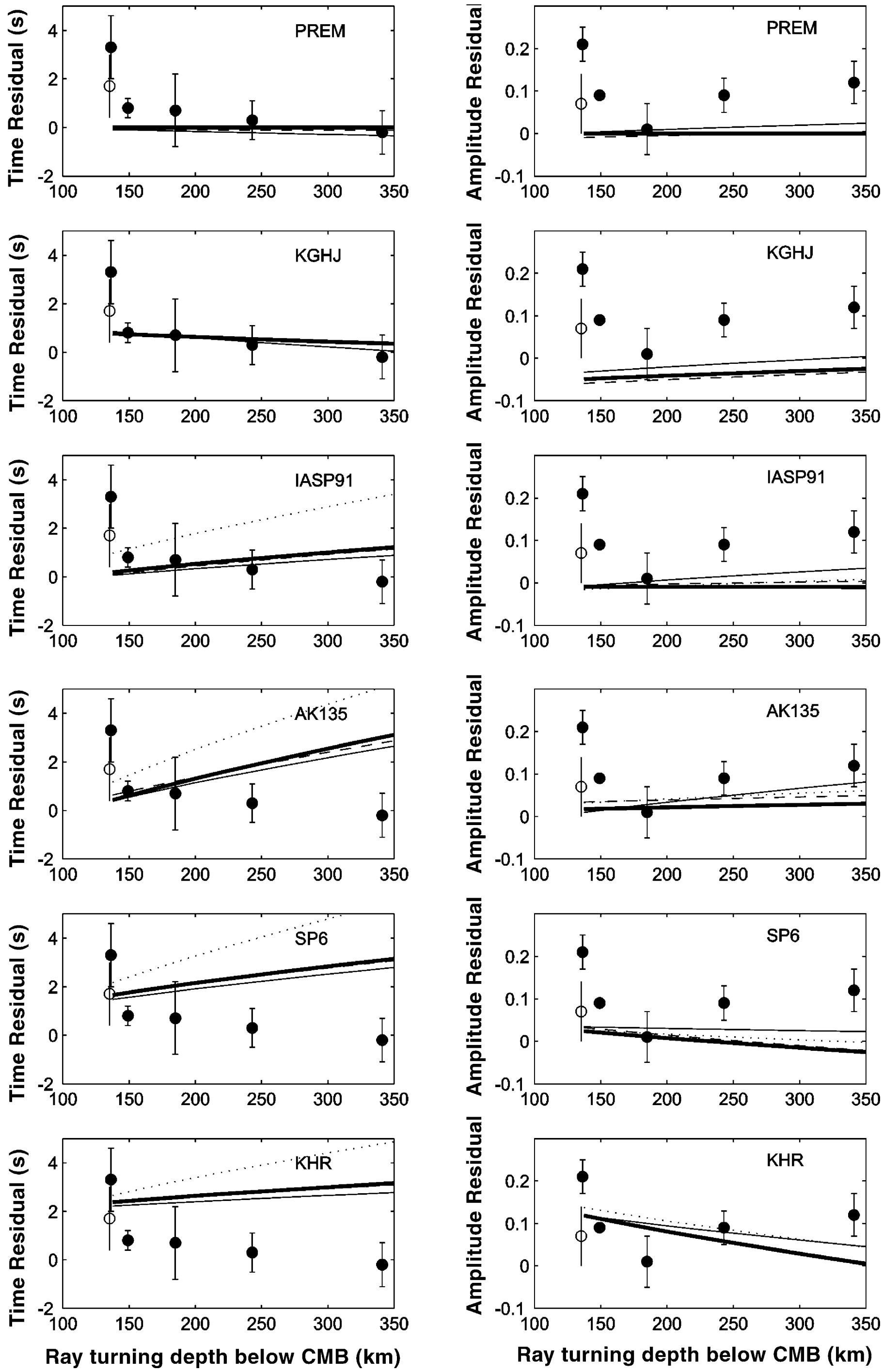

Fig. 13. Calculated $t_{S3KS} - t_{S2KS}$ time residuals (left) and amplitude residuals (right) with respect to PREM, compared with array observations from this study. Bold solid lines are for the reference model indicated in the top right corner of each graph. Thin lines show results obtained by inserting into each of the models a 12-km thick layer at the top of the outer core with properties of a light, immiscible S-rich liquid at 4300 K ($V_p = 8.36$ km/s, $\rho = 8.97$ Mg/m^3; Helffrich and Kaneshima, 2004). Dashed lines show results for a 12-km thick layer with a 10% reduction in ρ but no change in V_p. Dotted lines show results for a 12-km thick layer with a 10% reduction in both ρ and V_p. No picks were obtained in the latter case for models PREM and KGHJ due to severe waveform distortions caused by the low-velocity layer. Note improvement in fit from introduction of S-rich liquid, regardless of reference model.

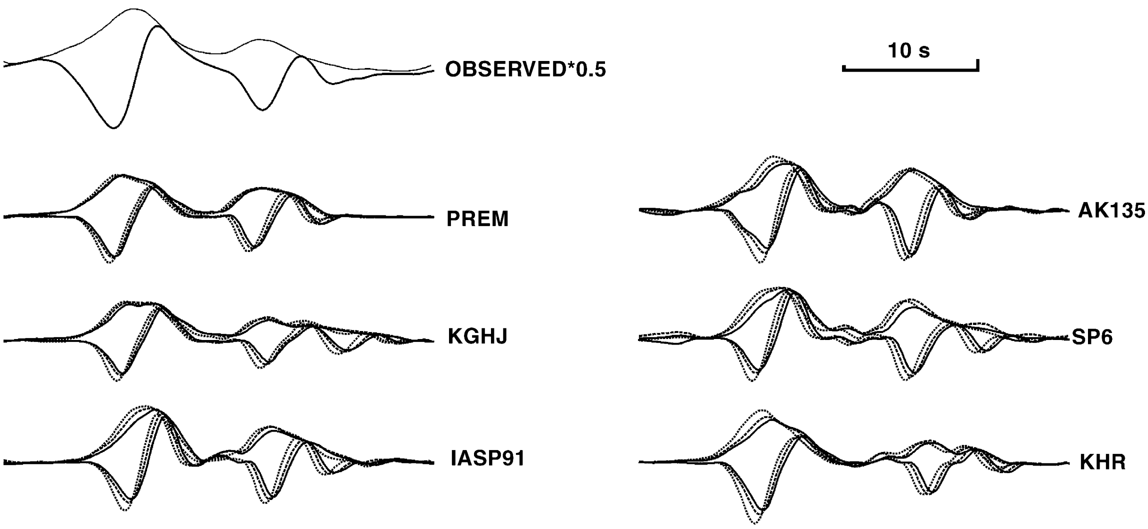

Fig. 14. Observed and synthetic seismograms showing *S3KS* and *S4KS** signals ($\Delta = 140.39°$). Amplitude-envelope traces are also shown. Synthetics were computed using source parameters for event 3. Seismic trace amplitudes are normalized with respect to the maximum amplitude of the *SKKSac* phase. Synthetics plotted with dashed and dotted lines were computed by inserting a layer at the top of the core of thickness 7 and 12 km, respectively, with properties of a light, immiscible S-rich liquid at 4300 K ($V_p = 8.36$ km/s, $\rho = 8.97$ Mg/m^3; Helffrich and Kaneshima, 2004). Insertion of this layer changes the phase of the waveforms, and increases the amplitudes of *S3KS* and *S4KS** relative to *SKKSac*.

phase-rotation of the pulse could provide another possible future test of this hypothesis.

To illustrate the sensitivity of the *SmKS* waveforms to lid thickness, Fig. 14 shows traces computed with both a 7-km thick and 12-km thick layer. The relatively subtle waveform differences for the 7-km thick layer suggests that this may be near the minimum layer thickness that can be resolved, for the dominant period (5 s) used in this example.

7. Conclusions

The analysis of *SmKS* phases provides a powerful method to investigate the fine-scale structure of the Earth's outermost core, where existing reference Earth models exhibit a large amount of scatter and where a thin low-density layer has been postulated to exist. Several previous studies have employed *SmKS*–*SnKS* ($n = m - 1$) time residuals to infer 1D velocity models for this region. Here, we build on this concept by introducing a simple frequency-domain deconvolution technique that uses the *SKKSac* waveform as a reference pulse. In the future this technique (also known as matched filtering) may be useful as a data-preparation step prior to the application of full-waveform inversion. We have also modified the vespagram method of Tanaka (2004), by applying an amplitude-envelope transformation to the seismograms prior to the array beam-forming process. Our approach facilitates the process of picking arrival times, since the amplitude envelope automatically accounts for Hilbert-transform phase shifts that are intrinsic to the *SmKS* sequence of pulses.

We have applied our methodology to Canadian broadband recordings of three recent deep-focus earthquakes. Our new data partly fill a gap in global coverage of *SmKS* phases with an average turning depth in the outermost 190 km of the core. The corresponding rays in our study enter and exit the Earth's core close to several major velocity anomalies in D″. To mitigate complications arising from interaction with lower-mantle velocity heterogeneity, we have focused on pairs of phases with core entry/exit points situated inside their mutual Fresnel-zone limits. With respect to PREM, our data exhibit a trend of decreasing time residuals with increasing turning depth, coupled with larger-than-expected *S3KS** amplitudes relative to *SKKSac*. Although some previously proposed models (e.g., model KGHJ of Garnero et al., 1993) fit our arrival-time data reasonably well, and others (e.g., model KHR of Hales and Roberts, 1971) fit the amplitude data reasonably well, none of the existing models considered here fit both types of data. We have examined the sensitivity of our array measurements to model perturbations, and find that a slight improvement in the fit arises for all models by the inclusion of a thin (12-km) high-velocity and low-density layer as proposed by Helffrich and Kaneshima (2004).

Acknowledgments

Most of this work was performed while D.W.E. was on sabbatical leave at the Dublin Institute for Advanced Studies (DIAS). Financial support and access to computation resources at DIAS are gratefully acknowledged. This work was supported by a Discovery Grant from the Natural Sciences and Engineering Research Council of Canada. The superb quality POLARIS recordings would not have been possible without the tireless contributions of the POLARIS technical team. Several of the figures were prepared using GMT software (Wessel and Smith, 1998). This manuscript benefited from constructive comments by George Hellfrich and two anonymous reviewers.

References

Bostock, M.G., Sacchi, M.D., 1997. Deconvolution of teleseismic recordings for mantle structure. Geophys. J. Int. 129, 143–152.

Braginsky, S.I., 1999. Dynamics of the stably stratified ocean at the top of the core. Phys. Earth Planet. Int. 111, 21–34.

Buffett, B.A., Garnero, E.J., Jeanloz, R., 2000. Sediments at the top of Earth's core. Science 290, 1338–1342.

Chernick, M.R., 1999. Bootstrap Methods: A Practitioner's Guide. Wiley, New York.

Choy, G.L., 1977. Theoretical seismograms of core phases calculated by frequency-dependent full wave theory, and their interpretation. Geophys. J. R. Astr. Soc. 51, 275–312.

Dubrovinsky, L., Dubrovinskaia, N., Langenhorst, F., Dobson, D., Rubie, D., Gessmann, C., Abrikosov, I.A., Johansson, B., Baykov, V.I., Vitos, L., Le Bihan, T., Crichton, W.A., Dmitriev, V., Weber, H.-P., 2003. Iron–silica interaction at extreme conditions and the electrically conducting layer at the base of Earth's mantle. Nature 422, 58–61.

Dziewonski, A.M., Anderson, D.L., 1981. Preliminary Reference Earth Model. Phys. Earth Planet. Int. 25, 297–356.

Eaton, D., Adams, J., Asudeh, I., Atkinson, G., Bostock, M., Cassidy, J., Ferguson, I., Samson, C., Snyder, D., Tiampo, K., Unsworth, M., 2005. Geophysical arrays investigate lithosphere and earthquake hazards in Canada. EOS 86 (17), 169–173.

Feder, T., 2003. Ambitious Earth sciences project aims to crack mysteries of continents. Phys. Today 56 (12), 32–34.

Fuchs, K., Müller, G., 1971. Computation of synthetic seismograms with the reflectivity method and comparison with observations. Geophys. J. R. Astr. Soc. 23, 417–433.

Garnero, E.J., 2000. Heterogeneity of the lowermost mantle. Annu. Rev. Earth Planet. Sci. 28, 509–537.

Garnero, E.J., Helmberger, D.V., Grand, S.P., 1993. Constraining outermost core velocity with *SmKS* waves. Geophys. Res. Lett. 20, 2463–2466.

Garnero, E.J., Helmberger, D.V., 1995. On seismic resolution of lateral heterogeneity in the Earth's outermost core. Phys. Earth Planet. Int. 88, 117–130.

Hales, A.L., Roberts, J.L., 1971. The velocities in the outer core. Bull. Seis. Soc. Am. 61, 1051–1059.

Helffrich, G., Kaneshima, S., 2004. Seismological constraints on core composition from Fe–O–S liquid immiscibility. Science 306, 2239–2242.

Kendall, J.-M., Sol, S., Thomson, C.J., White, D.J., Asudeh, I., Snell, C.S., Sutherland, F.H., 2002. Seismic heterogeneity and anisotropy in the western Superior Province, Canada: insights into the evolution of an Archaean craton. In: Fowler, C.M.R., Ebinger, C.J., Hawkesworth, Chris, J. (Eds.), The Early Earth; Physical, Chemical and Biological Development, vol. 199. Geological Society Special Publications, pp. 27–44.

Kennett, B.L.N., 2001. The Seismic Wavefield II: Interpretation of Seismograms on Regional and Global Scales. Cambridge University Press, Cambridge.

Kennett, B.L.N., Engdahl, E.R., 1991. Traveltimes for global earthquake location and phase identification. Geophys. J. Int. 105, 429–465.

Kennett, B.L.N., Engdahl, E.R., Buland, R., 1995. Constraints on seismic velocities in the Earth from traveltimes. Geophys. J. Int. 122, 108–124.

Lay, T., Young, C.J., 1990. The stably-stratified outermost core revisited. Geophys. Res. Lett. 17, 2001–2004.

Li, X.-Q., Nábelek, J.L., 1999. Deconvolution of teleseismic body waves for enhancing structure beneath a seismic array. Bull. Seis. Soc. Am. 89, 190–201.

Lister, J.R., Buffett, B.A., 1998. Stratification of the outer core at the core–mantle boundary. Phys. Earth Planet. Int. 105, 5–19.

Mégnin, C., Romanowicz, B., 2000. The shear velocity structure of the mantle from the inversion of body, surface and higher modes waveforms. Geophys. J. Int. 143, 709–728.

Morelli, A., Dziewonski, A.M., 1993. Body wave travel-times and a spherically symmetric P- and S-wave velocity model. Geophys. J. Int. 112, 178–194.

Müller, G., 1977. Earth-flattening approximation for body waves derived from geometric ray theory; improvements, corrections and range of applicability. J. Geophys. 42, 429–436.

Neal, S.L., Pavlis, G.L., 2001. Imaging P-to-S conversions with broadband seismic arrays using multichannel time-domain deconvolution. Geophys. J. Int. 147, 57–70.

Rost, S., Thomas, C., 2002. Array seismology: methods and applications. Rev. Geophys. 40, 1008, doi:10.1029/2000RG000100.

Souriau, A., Poupinet, G., 1991. A study of the outermost liquid core using differential travel times of SKS, SKKS and S3KS phases. Phys. Earth Planet. Int. 68, 183–199.

Souriau, A., Teste, A., Chevrot, S., 2003. Is there any structure inside the liquid outer core? GRL 30 (11), 1567, doi:10.1029/2003GL017008.

Stevenson, D.J., 1987. Limits on lateral density and velocity variations in the Earth's outer core. Geophys. J. R. Astr. Soc. 88, 311–319.

Sylvander, M., Souriau, A., 1996. Mapping S-velocity heterogeneities in the D$''$ region, from *SmKS* differential travel times. Phys. Earth Planet. Int. 94, 1–21.

Tanaka, S., 2004. Seismic detectability of anomalous structure at the top of the Earth's outer core with broadband array analysis of *SmKS* phases. Phys. Earth Planet. Int. 141, 141–152.

Tanaka, S., Hamaguchi, H., 1996. Frequency-dependent Q in the Earth's outer core from short-period P4KP/PcP spectral ratio. J. Phys. Earth 44, 745–759.

Taner, M.T., Koehler, F., Sheriff, R.E., 1979. Complex seismic trace analysis. Geophysics 44, 1041–1063.

Wessel, P., Smith, W.H.F., 1998. New, improved version of the Generic Mapping Tools released. EOS Trans. AGU 79, 579.